Inorganic Chemistry Communications 179 (2025) 114822

Contents lists available at ScienceDirect

Inorganic Chemistry Communications

journal homepage: www.elsevier.com/locate/inoche

Research Article

Design of dual-functional sensor and co-catalyst nanomaterial for photodegradation of metronidazole based on biomass carbon dots derived from pine bark

Saheed O. Sanni [a,b,*], Odunayo T. Ore [c], Ajibola A. Bayode [d], Stephen Sunday Emmanuel [f], Hamza Badamasi [g]

[a] College of Chemical Engineering, Sichuan University of Science & Engineering, Zigong 643000, China
[b] Department of Biotechnology and Chemistry, Vaal University of Technology, Private Bag X021, Vanderbijlpark 1900, South Africa
[c] Department of Chemical Sciences, Achievers University, P.M.B. 1030, Owo, Nigeria
[d] Department of Chemical Sciences, Redeemer's University, P.M.B. 230, Ede, Osun State, Nigeria
[f] Department of Industrial Chemistry, Faculty of Physical Sciences, University of Ilorin, P.M.B. 1515, Ilorin, Nigeria
[g] Department of Chemistry, Federal University, Dutse, Jigawa State, Nigeria

ARTICLE INFO

Keywords:
Biomass carbon dots
Metronidazole
Fluorescence sensor
$CoTiO_3$
Photodegradation
Central composite design

ABSTRACT

The health risk posed by metronidazole antibiotic in the environment necessitates a sustainable approach for its detection and degradation. A benign microwave pyrolysis approach was adapted for the fabrication of fluorescent biomass carbon dots (BCDs) from pine bark (PB) agro-waste, highlighting its dual functionality for metronidazole (MNZ) detection, and as a co-catalyst with $CoTiO_3$ (CTO) in MNZ degradation. The results demonstrated that the BCDs with diverse functional groups, was an effective fluorescent probe for MNZ detection, with fluorescence quenching at an emission of 430 nm under 330 nm excitation. The linear range for detection of MNZ was 0–25 μM with a detection limit as low as 0.014 μM. Additionally, rationally modifying BCDs on CTO resulted in the design of highly active BCDs/CTO photocatalysts, and the experimental results were modeled through a central composite design (CCD) under the response surface methodology (RSM) to predict and optimize MNZ photodegradation. At optimal operational conditions (pH = 9, MNZ = 64.17 mg/L, and 5.5 wt % catalyst loading), 99.81 % of MNZ was degraded within the 60 min irradiation time. The degradation rate constant of 5.5 wt% BCDs-CTO (0.0786 min^{-1}) surpasses that of CTO (0.0192 min^{-1}) and BCDs (0.0131 min^{-1}) by 4.1 and 6 times, respectively. The reusability of 5.5 wt% BCDs/CTO was assessed in five consecutive series, thus providing evidence of high stability and superior interaction of the BCDs, and CTO. The BCDs nanomaterial significantly contributes to the simultaneous sensing and degradation of MNZ, offering a promising solution to mitigate pharmaceutical pollution in aquatic environments.

1. Introduction

Pharmaceutical antibiotics are extensively utilized in our everyday life; however, they have emerged as a critical ecological issue aftermath of the COVID-19 pandemic, owing to their elevated release into the environment by households, improper management/disposal by hospitals, agricultural activities, and industries [1,2]. In particular, metronidazole (MNZ), as one of the most widespread antibiotics, has a close relationship with our lives for the treatment/prevention of potentially harmful ailments [3,4]. Though the excessive presence of MNZ residues and metabolites in soil and water is persistent and naturally resistant to degradation, it indirectly impacts the environmental system and higher medical costs [5]. This overtime has been associated with appetite loss, headache, hormonal imbalance, blurred vision, and seizures [6–8]. The conventional water treatment's seriously failed at removing MNZ in the environment. Hence, there is a significant requirement to formulate and construct a straightforward, expeditious, dependable nanomaterial with dual-functional solutions for the detection and remediation of MNZ in water samples.

Currently, analytical methods comprising high-performance liquid chromatography [9], thin-layer chromatography [10], supercritical fluid chromatography [11], ultraviolet (UV) spectroscopy [12],

* Corresponding "author.
E-mail address: mosqit.saheed@gmail.com (S.O. Sanni).

https://doi.org/10.1016/j.inoche.2025.114822
Received 5 December 2024; Received in revised form 15 May 2025; Accepted 31 May 2025
Available online 6 June 2025

colorimetric [13], electrochemical method [14], and fluorometric spectroscopy have been explored to detect MNZ in water samples. Fluorescence spectroscopy has emerged as a prevalent technique in contemporary times for the detection of MNZ antibiotics on account of their remarkable sensitivity and nonintrusive characteristics [3,15–17]. Fluorescent probe sensors, such as semiconductor quantum dots, gold nanoclusters, luminescent metal–organic frameworks, and carbon nanomaterials, have been specifically engineered to detect antibiotics in aquatic environments [1]. Fluorescent carbon nanomaterials-based systems, especially carbon dots (CDs), among the highlighted sensors not only presented distinctive features, comprising good water solubility, lesser cytotoxicity, high-level biocompatibility, high emission quantum yield, controllable optical attributes, eco-friendly nature for sensing, and remediation applications [18–21]. Recently, agricultural waste, and biomass from Trapa bispinosa peels [22], orange peel [23], Putrescent garlic (Allium sativum) [24], coconut petiole residues [25], and Ginkgo biloba [26] have received commendable attention as CDs fabrication precursors, compared to the utilization of chemicals, and other organic substances. This is largely attributed to the low-cost, nontoxicity, renewable nature, and greener nature of the agricultural materials [27]. Nitrogen-doped carbon dots (N-CDs) derived from chicken biowaste via hydrothermal synthesis (240 °C for 8 h), have been innovated to detect MNZ [28]. CDs derived from Gardenia jasminoides were prepared via the hydrothermal approach (180 °C for 6 h), and its fluorescent detection of MNZ was untaken [16]. These studies reported good accuracy, high sensitivity, and low detection limit, but were limited by mono-functional detection of MNZ, and the absence of further fair remediation of the antibiotic in groundwater. Since the utilization of a single CDs nanomaterial as a sensor of MNZ alone cannot provide maximum potential for commercial-scale applications, extensive removal from the ecosystem using an affordable remediation technique is warranted.

Cobalt titanate ($CoTiO_3$) a typical ABO_3-type perovskite, has attracted considerable attention in remediation purposes under the heterogeneous photocatalysis technology. Notably, its narrow energy bandgap (Eg = 2.25 eV), good magnetic properties, and outstanding photochemical stability, thus rendering the $CoTiO_3$ nanoparticles (NPs) applicability in magnetic recording, gas sensors, pigment, dielectric material, and catalysis [29,30]. However, pure $CoTiO_3$ exhibits reduced photocatalytic capability, largely attributed to reduced visible light absorptivity, low electron mobility, and a recombination rate of photogenerated charge carriers [31,32]. Nanocomposites based on the $CoTiO_3$, comprising Ti/$CoTiO_3$/Ce-PbO_2 [33], $CoTiO_3$@Co_3O_4/N-CNO [34], $CoTiO_3$/TiO_2 [35], and Fe-doped $CoTiO_3$/SiO_2 [36], have prepared to enhance photocatalysis applications, still unsatisfactory because of their limited ability to use the solar spectrum, and avert photogenerated charge carriers recombination. Hence, green and synergistic bonded $CoTiO_3$ heterojunctions must be developed to promote their practicality. The utilization of carbon dots (CDs) nanomaterial has triggered intensive interest in various redox reactions with ilmenite heterojunctions in the remediation of organic pollutants solely [37,38], whilst neglecting the integrated systems. The utilization of CDs with an adequate energy gap, electron storage, and carrier separation capacity [39,40] will greatly boost the photocatalytic performance of the $CoTiO_3$ catalyst. Thus, decorating $CoTiO_3$ with CDs can effectively address the setback of the photocatalyst $CoTiO_3$ material, facilitate tight interface contact [41], a large formation of active sites, and thus significantly improve the photocatalytic performance of the heterojunction for remediation purposes.

In taking advantage of naturally abundant materials as precursors for CDs synthesis, high-value-added utilization of Pine bark is still underrated. The chemical structure of the fully-fledged pine bark is comprised of cellulose, hemicellulose, and lignin, which have found application as a good precursor for carbon nanomaterial synthesis [42,43]. Hence, the utilization of underused pine bark in the fabrication of high-value CDs thus serves environmental protection, economic benefits for speedier detection of MNZ, and as a co-catalyst with $CoTiO_3$ in the antibiotic remediation, which is highly warranted, since such studies have not been carried out before. It is imperative to emphasize that prior studies involving carbon nanomaterials with ilmenite catalysts have not incorporated multi-parameter optimization in the photo-oxidation of organic pollutants. The current study addresses these aforementioned gaps in CDs production via a greener method, utilizing it as a sensor and a co-catalyst for $CoTiO_3$ by exploring the RSM-CCD (Response Surface Methodology- Central Composite Design) in the degradation process.

Herein, highly fluorescent biomass carbon dots (BCDs) were successfully synthesized from pine bark, through a green and facile microwave pyrolysis method. We have utilized a microwave pyrolysis approach for BCDs design, thus saving more reaction time and energy generation, as another alternative to previous studies reported in the sensing of MNZ [44]. We comprehensively analyzed the BCDs morphology, structure, and optical attributes. The fluorescent BCDs probe selective quenching with MNZ, evidenced high sensitivity, and presented a better limit of detection (LOD), compared with previously reported studies. Furthermore, the $CoTiO_3$ (CTO) modified with BCDs was designed by the Pechini protocol [37], and then applied for photodegradation of MNZ following the RSM-CCD pathway. The crucial degradation parameters of the photocatalytic process, including catalyst loading, pH solution, and MNZ initial concentration, were optimized using RSM-CCD and quantified. The BCDs-CTO nanocomposite strongly degrades MNZ antibiotic residues after exposure to light illumination for approximately 1 h (99.80 %), thus evidence the heterojunction versatility for redox reactions.

2. Materials and methods

2.1. Reagents

Sulfamethazole (SMZ), chloramphenicol (CLM), tetracycline (TC), metronidazole (MNZ), ciprofloxacin (CIP), and ethanol were all obtained from Merck Chemicals. Nitrate salts of Cadmium, zinc, Iron (III), Iron (II), nickel, mercury, cobalt (II) nitrate hexahydrate, titanium (IV) isopropoxide, citric monohydrate acid, and Rhodamine B (99 %) were acquired from Sigma-Aldrich.

2.2. Synthesis of biomass carbon dots (BCDs)

Biomass CDs were rapidly synthesized by using pine bark (PB) obtained from Vaal University of Technology, South Africa as starting precursor, through the microwave pyrolysis method. Firstly, the chopped, sieved PB was put into a 250 mL Duran quartz bottle, and then subjected to pyrolysis inside a microwave oven (model LG MH8042GM, maximum power of 1000 W at a frequency of 2450 MHz) for 30 min at 800 W with periodic cooling in each 5 min under inert atmosphere through purging of nitrogen gas. After that, a Branson 2800 sonication water bath was used to sonicate 3 g of charred PB powder mixed with 150 mL of ultrapure water for 30 min. The mixture was then centrifuged for 60 min at 10,000 rpm, the supernatant was filtered through a 0.22 m filter membrane, and the biomass CDs powder was obtained by freeze-drying. (SCANVAC CoolSafe™).

2.3. Synthesis of Cobalt titanate, and BCDS −Cobalt titanate (BCDs-CTO) photocatalysts

The modified Pechini method, which is similar to that which was previously reported, was used to design BCDS-CTO catalysts [37]. To a 50 mL ethanol, citric acid (0.06 mol), and Cobalt (II) nitrate hexahydrate (0.01 mol) were introduced. Then, 0.01 mol titanium (IV) isopropoxide was slowly added to the stirred solution and further stirred for 2 h. Then, this mixture was transferred, and heated for 2 days at 80 °C in an electric oven. The gel was further calcined at 600 °C for 4 h, and after cooling the obtained powder was milled into a fine powder in an agate mortar.

The BCDs-CTO photocatalysts were synthesized using the wet chemical approach, whereby 300 mg of as-prepared CTO and different specific amounts of BCDs were dispersed into absolute ethanol. The mixture was subjected to stirring, and sonicated for a period of 8 h, and then the slurry was centrifuged and dried at 80 ∘C for 12 h in a vacuum oven. The residue material was labeled as x-BCDs-CTO, where "x" represents the quantity of BCDs added (x = 3 wt%, 5.5 wt%, and 8 wt%). This loading amount is specifically carried out in line with the RSM-CCD design.

2.4. Characterization

The morphology and particle size of the BCDs and BCDs-CTO photocatalyst were recorded by Tecnai 20 transmission electron microscope and Scanning Electron Microscopes (SEM) ZEISS Ultra/Plus FEG-SEM. The functional group was performed with a Fourier transform infrared spectrometer (Perkin Elmer spectrum 400). X-ray diffraction (XRD) patterns for BCDs, and BCDs-CTO photocatalyst were recorded with a Bruker diffractometer AXS with Cu kα radiation source. Raman spectra were measured by a Horiba LabRAM HR Evolution (Kyoto, Japan). The UV–vis absorption spectrum and fluorescence spectrum of the BCDs were detected using a Maya 2000 Ocean Optics spectrometer and Jasco FP-8600 spectrophotometer, respectively. Thermal analysis with a heating rate of 10˚C/min in a nitrogen purge stream from 30 to 900 °C under 19.8 mL/mins was performed by Perkin Elmer STA 6000 thermal simultaneous analyzer. Cyclic voltammetry (CV), and electrochemical impedance spectroscopy (EIS) were performed using Bio-Logic SP-300 potentiostat (ferrocyanide solution) with a three-electrode cell system (glassy carbon electrode as the working electrode, Ag/AgCl served as the reference electrode, and platinum (pt) as the counter electrode).

2.5. Fluorescence quantum yield measurement

The fluorescence quantum yield and fluorescence MNZ measurement are given in the *supplementary information (SI)* (Text S1).

2.6. Photocatalytic activity test

The photocatalytic performance was evaluated by degrading MNZ, and the degradation details are presented in *SI* (Text S2).

3. Results and Discussion

3.1. Preparation and characterization of BCDs

Pine bark (PB) was utilized as the raw material to synthesize green biomass carbon dots (BCDs), using a microwave technique (Scheme 1), thus eliminating the necessity for a complex preparation process and chemical additives. The synthesized BCDs showcased the highest fluorescence excitation at 330 nm and the maximum emission at 430 nm (as further emphasized in ***section 3.2***).

The morphology of BCDs, as assessed by TEM (Fig. 1**A**), was spherical in morphology and well dispersed, without aggregation. The histogram data (Fig. 1**C**) shows that the BCDs possess an average size distribution within the range of 1.5 to 60 nm, with an average particle size of 18.39 nm. The BCDs (Fig. 1**B**) showed that the lattice spacing is approximately 0.23 nm and ascribed to the (1 0 0) plane characteristic of regular graphite [45].

XRD powder pattern of BCDs displayed a broad diffraction signal at 22.5, and a weak peak at 43.3°, which aligns with 002, and 101 lattice planes, thereby evidencing the amorphous and graphitic carbon structure [46–48] in the prepared BCDs (Fig. 1**D**). The Raman spectrum of the BCDs as presented in Fig. 1**E**, comprises two peaks positioned at 1363

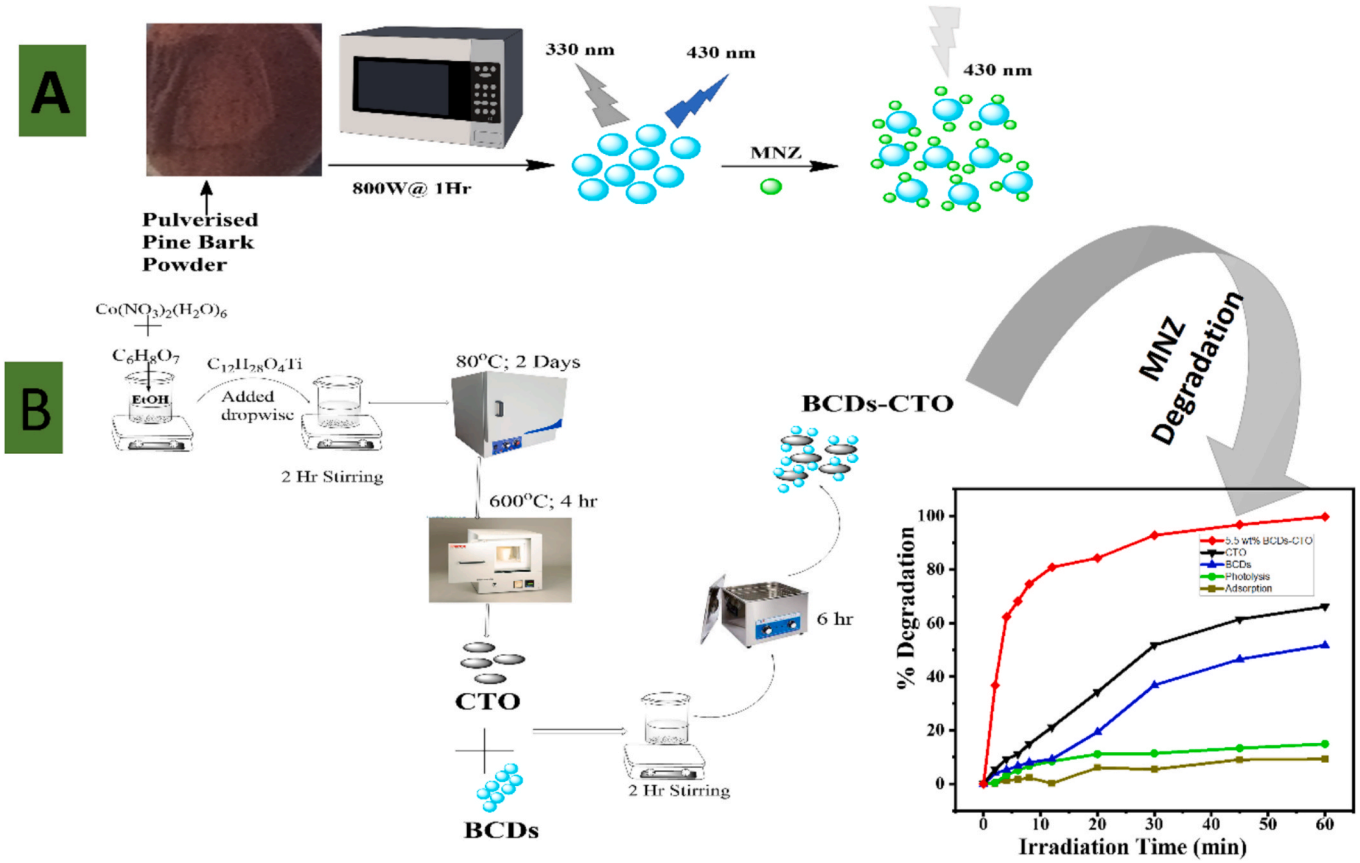

Scheme 1. Design process of (A) BCDs, and (B) BCDs-CTO photocatalysts.

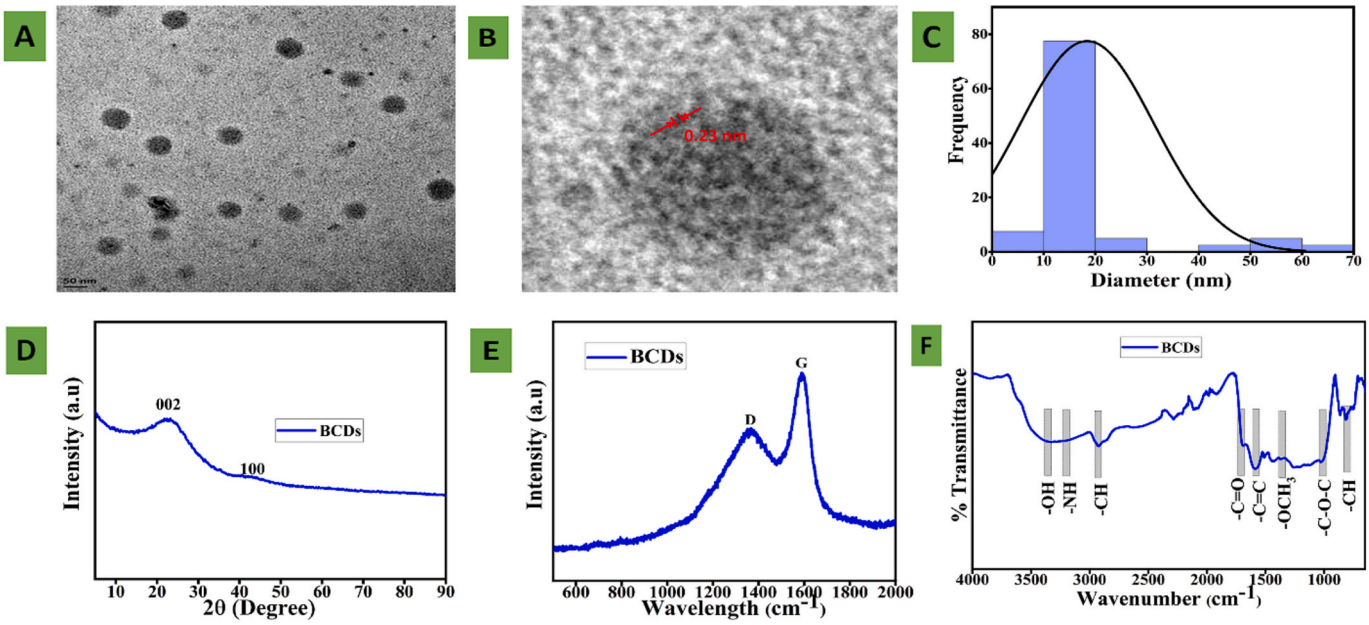

Fig. 1. (A) TEM image (B) HRTEM image, (C) Particle size distributions, (D)XRD pattern, (e) Raman plot, and (F) FTIR spectra of BCDs.

cm^{-1} and 1585 cm^{-1}, which align to the D band (structurally disordered) and G band (graphite phase), respectively [49]. The I_D/I_G ratio was determined to be 0.85, thus affirming that the BCDs possess a strong degree of graphitization nature, which further aligns with the XRD result.

The FTIR spectrum of BCDs was carried out, and presented in Fig. 1**F**. This figure evidenced the formation of –OH broad peak, and –NH stretching vibrations at 3398 cm^{-1}, and 3170 cm^{-1}, respectively thus suggesting the hydrophilic attributes of BCDs [50]. Also, peaks at 2914 cm^{-1} and 815 cm^{-1} were assigned to the –CH stretching vibration [51–53]. Additionally, the peaks at 1696 cm^{-1} and 1577 cm^{-1} evidence the C=O [54], and C=C stretching vibration that is present in the BCDs sample [55]. The peaks observed at 1427 cm^{-1}, and 1031 cm^{-1} represent the $–OCH_3$ [56] and symmetric stretching vibrations of the C-O-C group, respectively. The BCDs surface functionalities primarily centered on diverse functional groups.

The BCDs sample thermal analysis (TG, and DTG) as presented in Fig. S1, exhibited a total weight loss of about 20 %, thus indicating the material was relatively stable. At first, we have initial weight loss between 30 to 180 °C occur, which is attributed to the evolution of surface-adsorbed water molecules and light volatiles [57]. In addition, major weight loss between 200–480 °C is associated with the devolatilization

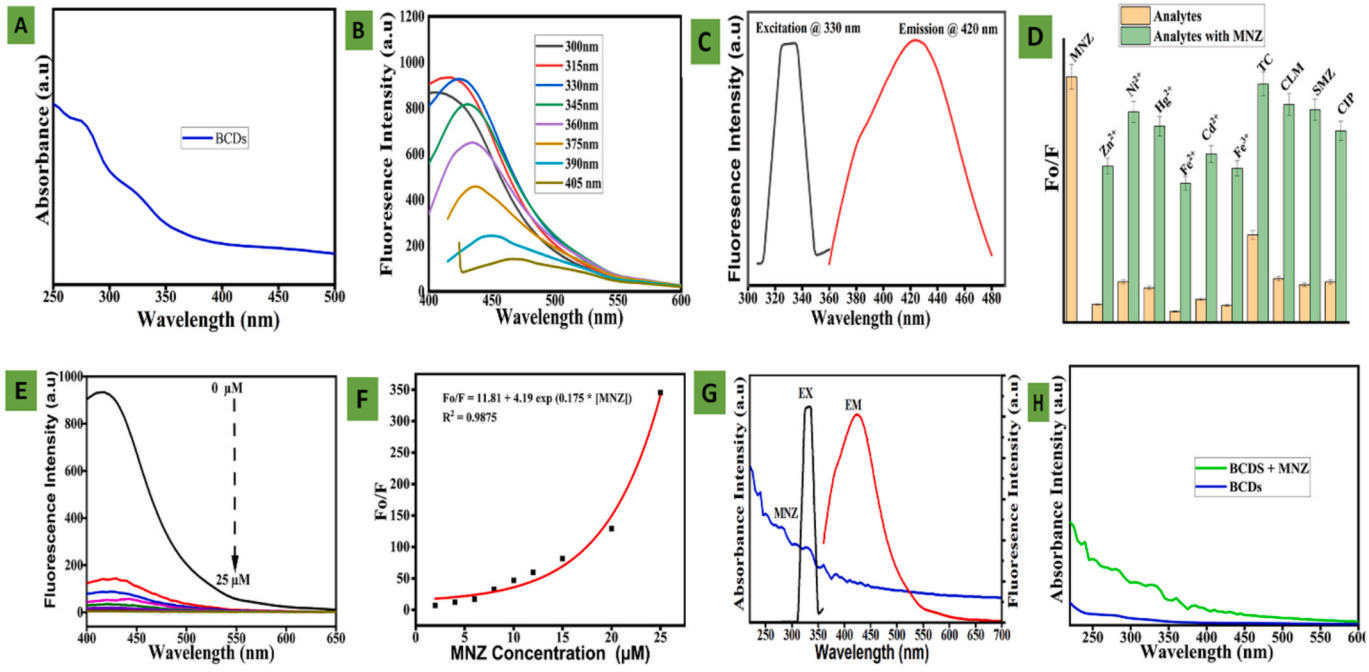

Fig. 2. (A) UV–Vis, (B) fluorescence emission spectra of the BCDs at different excitation wavelengths from 300 to 405 nm, (C) fluorescence excitation/emission spectra, (D) the effect of interference substances, (E) fluorescence intensity quenching of BCDs with MNZ concentration (0–25 µM), (F) Plot of relative fluorescence F_0/F intensity with metronidazole solution, (G) UV–vis spectrum of MNZ and fluorescence excitation/emission spectra of BCDs, and (H) UV–vis absorption of BCDs and BCDs that mixed with MNZ.

of the BCDs, and pyrolytic degradation of functional groups formed on the surface of BCDs [58]. The last stage (above 500 °C) involves the detachment of the graphitic structure occurs [59].

3.2. Optical properties of BCDs

The optical characteristics and photoluminescence (PL) of the BCDs were inspected using UV–Vis spectroscopy and fluorescence spectroscopy (Fig. 2). From the UV–Vis absorption spectra as presented in Fig. 2**A**, there are two absorption peaks, one at 277 nm (sharpen absorption peak) and a shoulder peak around 325 nm. These peaks are attributed to $\pi \rightarrow \pi^*$ transition of C=C bands, and $n \rightarrow \pi$ electronic transition of C=O bands in synthesized BCDs [60,61]. The BCDs with different luminescence attributes from 300 to 405 nm are found in the fluorescence emission spectra, as presented in Fig. 2**B**. The BCDs emission spectra were red-shifted between the range of 400 to 500 nm with an increasing excitation wavelength, accompanied by a decrease in the fluorescence intensity. This further affirms that the fluorescence properties of BCDs are powerfully dependent on the excitation wavelength, in addition to the varying size of the CDs and different surface states [51,62]. The fluorescence spectrum of BCDs exhibited a maximum emission intensity upon excitation at 330 nm (Fig. 2**C**) and was higher than the emission peak acquired when excited above the range of 360 to 405 nm. Furthermore, the quantum yield of BCDs using rhodamine B as a standard (from **eqn S1**) was approximated at 10 % for the emission spectra at 430 nm.

Considering the extensive application of the CDs within a complex practical setting, the stability of BCDs was assessed through the examination of their fluorescence intensity at varying pH values, irradiation under UV light, and after several days. With the pH ranging between 2 and 10, the fluorescence intensity of the BCDs remained the same (exhibited minimal change in wavelength) (Fig. S2A). However, the fluorescence emission intensity (Fig. S2A and S2B) significantly declined with pH change, as high emission intensity was observed at lower pH (<5), and the fluorescence intensity was reduced at higher pH (> 4). The highest quenching efficiency of BCDs occurred at pH 6. In addition, under extreme pH conditions, the accumulation of BCDs from enhanced non-covalent bond interactions like hydrogen bonds between hydroxyl, carboxyl, and amino functional groups [55,63,64], provide favorable protonation-deprotonation in different acid, and alkaline solutions. The variation in the pH medium also results to a photobleaching process related to fluorescence reduction [65]. Following a 240 min exposure to UV irradiation, the fluorescence intensity of the BCDs remained nearly identical to the initial intensity, thus demonstrating the superior resistance of the BCDs to photobleaching (Fig. S2C). Moreover, the fluorescence intensity experienced unaltered fluctuations under normal light irradiation after 25 days (Fig. S2D). In summary, the BCDs possessed a remarkable ability to adapt to diverse environmental conditions, thereby providing a dependable platform for the promising utilization of this fluorescent probe in real-world scenarios. The developed method was validated following the guidelines outlined in ICHQ2(R1) to ascertain its dependability and precision [66].

3.3. BCDs application in MNZ sensing

The selectivity of the BCDs fluorescent probe was tested, and the effects of various metal ions (Fe^{2+}, Fe^{3+}, Zn^{2+}, Ni^{2+}, Hg^{2+}, and Cd^{2+}), and pharmaceutical antibiotics (SMZ, CLM, TC, and CIP), utilized for agricultural activities inclusive of MNZ were investigated on fluorescence responses of BCDs.

As shown in Fig. 2**D**, our BCDs critically responded well to the pharmaceutical antibiotics (with higher fluorescence emission intensity), specifically to MNZ, highlighting the high selectivity for MNZ antibiotic identification. Furthermore, the *Fo/F* values of these samples are presented in Fig. 2**D** (herein *F* is the fluorescent intensities of each sample without BCDs, while *Fo* is the fluorescent intensity of BCDS without adding the sample). The results indicate that the high *Fo/F* value of MNZ (96 %) to lower values of other samples, evident that BCDS had a lower fluorescence emission intensity owing to the MNZ's quenching effect on the sensor. The interference experiments were conducted by mixing MNZ and other interferents (100 μM) found in wastewater. However, the addition of MNZ, along with each interferent did significantly influence the quenching of BCDs, and display any obvious effects as presented in Fig. 2**D**. Clearly, the BCDs were insensitive to other contaminants but selective to MNZ in the mixtures. This observation highlights BCDs exceptional sensitivity, excellent selectivity, and anti-interference attributes for MNZ detection.

For the sensitivity study of BCDs, 0–25 μM MNZ concentrations were investigated by recording the fluorescence intensity of BCDs. The spectra image of BCDs as presented in Fig. 2**E** shows the fluorescence intensity quenching 430 nm associated with MNZ concentrations augmentation, without any change in the emissive spectra. It emphasizes that the BCDs system is sensitive to the MNZ concentration. Herein, the *Fo/F* value of synthesized BCDs is MNZ-concentration-dependent, with increasing MNZ concentrations as displayed in Fig. 2**F**. The fluorescence quenching of the BCDs in the presence of MNZ aligned with the modified Stern–Volmer expression [67]. The curve fitted a non-linear exponential decay in line with the previously reported study [55,68], whilst the $F_0/F = 11.81 + 4.19 \exp 0.175^*$ [MNZ], with a correlation factor (R^2) of 0.9875. The limit of detection (LOD, at the signal-to-noise ratio of 3) of BCDs as calculated from the non-linear curve was estimated to be 0.014 μM. The detection limit was lower, and comparable to previously reported on MNZ sensing as presented in Table 1. The BCDs probe for MNZ sensing in this work exhibits numerous dominant behaviors compared to similar reports as presented in Table 1, comprising the environmentally friendly pyrolysis using a microwave oven that does not require any hazardous chemicals. The microwave pyrolysis of pine bark biomass for the development of BCDs, also requires a simple separation process, thus saving energy and time.

3.4. Florescence quenching of MNZ

As evidenced earlier, the fluorescence attributes of BCDs were significantly quenched upon the addition of MNZ to our fluorescent probe. Hence, to understand the proper nature of quenching, a refined approach is discussed using the UV–vis absorption analysis of fluorescent probe, MNZ, and a combination of the probe along with MNZ in line with existing literature [4,53,56]. MNZ weak peak from the UV–vis spectra was observed to have overlapped with the excitation spectrum of BCDs (Fig. 2G), and Fig. 2**H** portrayed a significant enhanced absorption with the introduction of MNZ. Herein, no new formation of complex or electron-hole recombination was achieved between the fluorescent probe and the organic compound. Then the overall fluorescent mechanism thus aligns with the inner filter effect (IFE) [3,4,70].

3.5. Analytical application of MNZ in real water samples

To examine the reliability of the BCDs fluorescent probe in practical settings, we employed it to detect the recovery ratios by introducing various concentrations of MNZ (from 0.5 μM, 2 μM, and 3 μM) into real water samples (tap water, and river water), obtained from "Vaal University of Technology" environment. The results presented in Table S1 reveal that by utilizing the BCDs fluorescent probe, we effectively identified the presence of MNZ antibiotics in the spiked tap water and river water. Notably, the recoveries of MNZ ranged from 97 % to 105 %, with a relative standard deviation (RSD) of less than 5 %, thus our findings suggest that the developed BCDs fluorescent probe is a reliable and suitable candidate for the determination of MNZ in actual environmental water samples.

Table 1
Comparison of different CDs for sensing of MNZ.

Carbon Precursor	Synthesis method (Conditions)	Linear range (μM)	Quantum Yield (%)	Selectivity LOD (μM)	Ref.
Non-conjugated polymer carbon dots (PCDs) from polyethyleneimine	HT (180 °C, 30 min)	0.06–15	9	0.020	[69]
Nitrogen-doped carbon dots (N-CDs) from L-tartaric acid and triethylenetetramine mixture	MWP (800 W, 6 min)	0.5–22	31	0.220	[70]
N-CDs from Galli Gigerii	HT (240 °C, 8 hr)	0–1000	19.45	0.267	[28]
N, S, P-Triple Doped Porous Carbon from *Elaeagnus gum*	HT (2 steps 130 °C for 6 hr; 750 °C for 3hr under N_2 atm.)	0.1–45 and 50–350	n.m.	0.013	[71]
N-CDs from mixture of citric acid and urea	HT (190 °C, 6 hr)	0–179	35	0.250	[72]
Bismuth-doped carbon quantum dots	HT (200 °C, 4 hr)	0.02–2	n.m.	0.016	[73]
Biomass carbon dots (BCDs) from pine bark	MWP	0 – 25	10	0.014	This Work

HT = Hydrothermal, N_2 = Nitrogen, Atm = Atmosphere, MWP = Microwave pyrolysis, n.m. = not mentioned.

3.6. Morphological and structural analysis of BCDs-CTO photocatalysts

Fig. 3A–C shows the SEM images of the active 5.5 wt% BCDs-CTO at different magnifications. The photocatalyst is composed of regular and slightly agglomerated spherical clusters with a large number of nanoparticles, and the BCDs are wrapped around the CTO nanoparticles (NPs), thus confirming synergistic interaction. In Fig. 3D and E**, 5.5** wt% BCDs-CTO TEM images showed a spherical structure of CTO comprising minute BCDs nanoparticles wrapped around, consistent with the SEM image.

The phase structures of the as-prepared CTO and BCDs-CTO nanomaterial (NM) were obtained by XRD (Fig. 3**F**). The distinct diffraction peaks of CTO can be found at 23.92^0 (012 plane), 32.80^0 (104 plane), 35.38^0 (110 plane), 40.59^0 (113 plane), 48.99^0 (024 plane), 53.52^0 (116 plane), 61.89^0 (214 plane), and 63.50^0 (300 plane). All are indexed to the ilmenite $CoTIO_3$ (JCPDS no. 15–0866), respectively [35]. No other crystalline phase can be detected. No signal of BCDs can be detected, primarily from low BCDs loading in the composite.

Fig. 3**G** shows FTIR spectra of CTO and 5.5 wt% BCDs-CTO photocatalyst. Both samples exhibited typical absorption peaks at 3340, 2923, 1610, 1450, and 1037 cm^{-1}. These peaks are attributed to the –OH stretching vibration, skeletal vibration of the sp^2 –CH band, C=O stretching band, $–OCH_3$, and C–O-C stretching vibration mode. Of note, the –CH, and $–OCH_3$ peaks were reduced with BCDs-CTO photocatalyst, thus affirming a significant change in the fundamental structure of CTO after the incorporation of BCDs. Also, the BCDs-CTO photocatalyst displayed the stretching mode of Ti–Co bonds appeared at 1037 cm^{-1} [74,75].

The TGA curve of CTO and 5.5 wt% BCDs-CTO photocatalyst is presented in Fig. 3**H**. Both samples exhibited typical weight loss at temperatures between 30 and 200 °C, and were assigned to water molecule loss. The 5.5 wt% BCDs-CTO remained relatively stable afterward without any further weight loss, whilst the CTO still underwent weight loss at 851 °C, and was assigned to the formation of ilmenite $CoTiO_3$.

X-ray photoelectron spectroscopy (XPS) analysis was conducted to analyze the molecular structure and atomic valence states of 5.5 wt% BCDs-CTO. As presented in Fig. 4**A**, XPS survey spectra of 5.5 wt% BCDs-CTO evidence Co, Ti, O, and C elements, without additional impurities. The Co 2p peak as presented in Fig. 4**B** evidences two states, namely: $2p_{3/2}$ and $2p1_{/2}$ states. The $2p_{3/2}$ state was identified at 780.45 and 786.8 eV, whilst the 2p1/2 was observed at 796.2 eV and 802.9 eV, respectively, thus evidencing the presence of Co^{2+} [76,77]. The Ti 2p (Fig. 4**C**) core levels also presented $2p_{3/2}$ and $2p_{1/2}$ states, with peaks

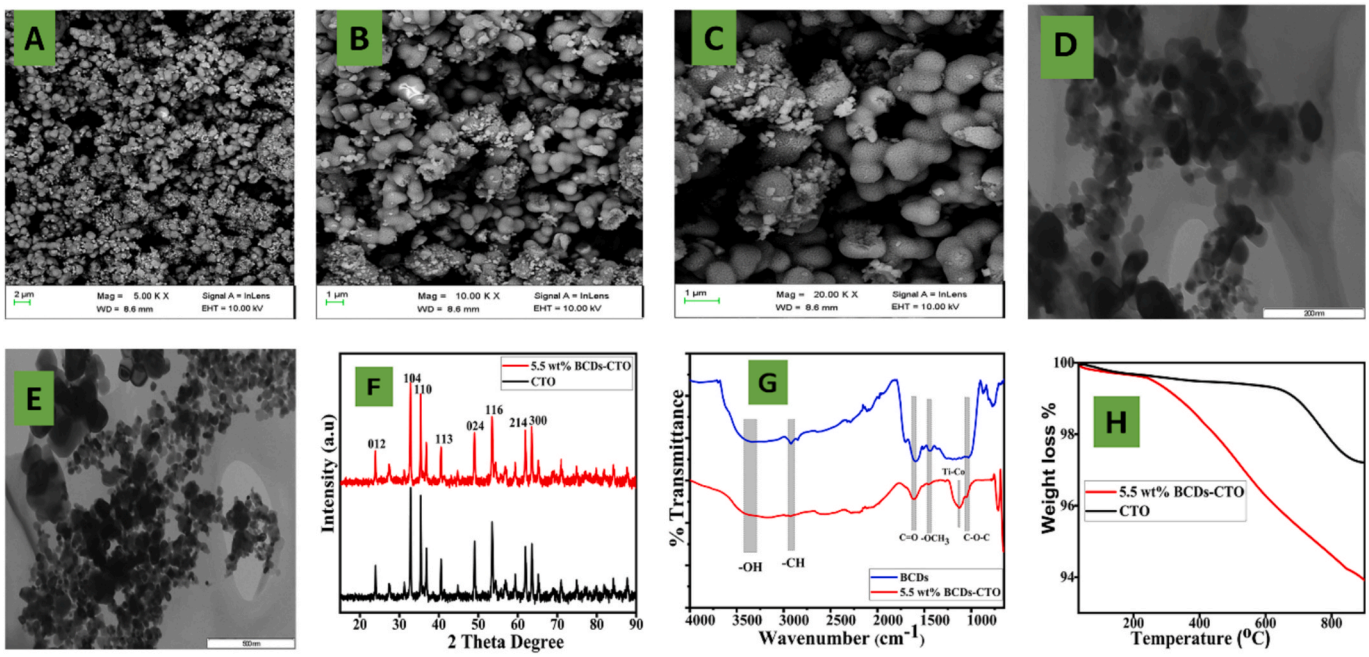

Fig. 3. (A–C) SEM images, (D, E) TEM images of 5.5 wt% BCDs-CTO sample at different magnifications, (F) XRD patterns, (G) FTIR spectra, and (H) Thermal analysis of 5.5 wt% BCDs-CTO, CTO, and BCDs samples.

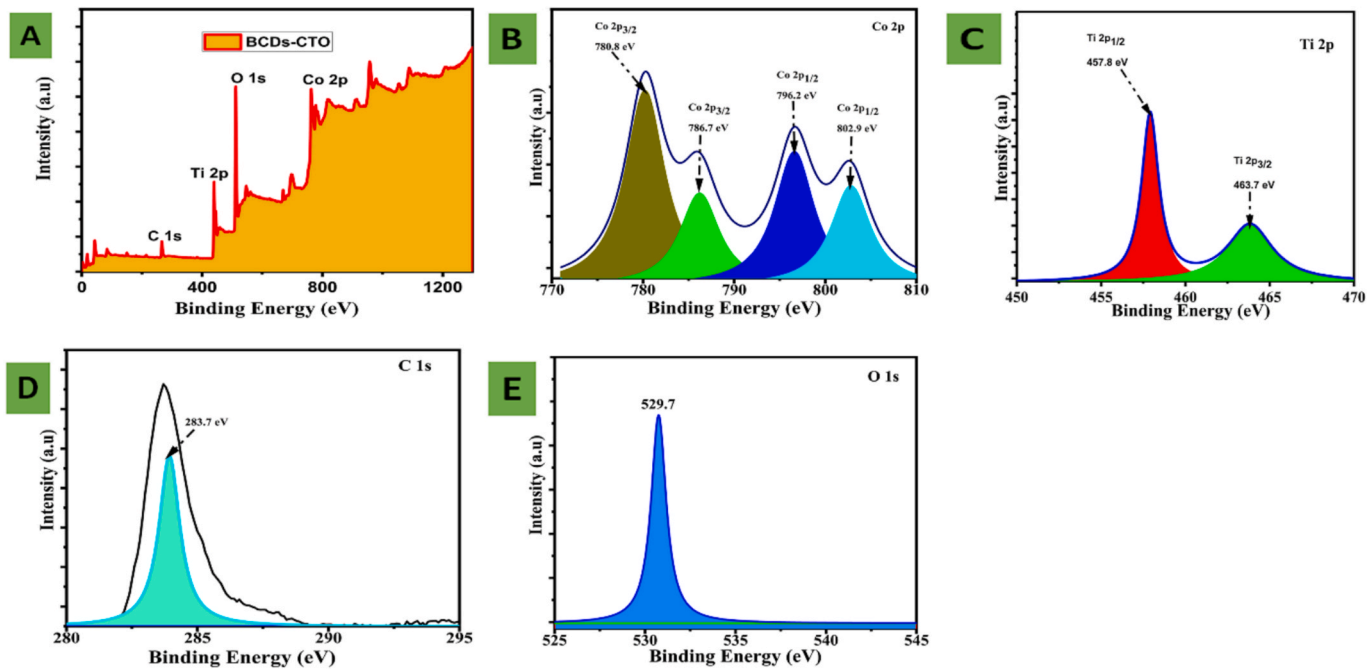

Fig. 4. (a) XPS survey plots with the individual spectra for 5.5 wt% BCDs-CTO aligning with (b) Co, (c) Ti, (d) C, and (e) O.

around 463.7 and 457.8 eV and thus affirm Ti^{4+}. The O 1s peak identified at 529.7 assigned to the lattice oxygen and the surface adsorbed oxygen species [78]. The C 1s peak at 283.7 eV is aligned with C–C bonding. The above analysis results provide significant evidence that CTO and BCDs are closely connected, and the preparation of the BCDs-CTO composite material is successful.

3.7. Photoelectric characteristics

The light absorption property of pure CTO and the BCDs-CTO photocatalysts is shown in Fig. 5**A**. The CTO NM presented intense absorption bands (491 nm, 579 nm, and 655 nm) in the whole spectral region. The absorption edge at 491 nm is assigned to the $O^{2-} \rightarrow Ti^{4+}$ metal-to-ligand charge transfer transition [77,79]. In addition, the $Co^{2+} \rightarrow Ti^{4+}$ charge transfer bands created by $CoTiO_3$ crystal field splitting or the d-d transition of Co^{2+} are attributed to the absorption edges detected at around 579 nm and 655 nm, respectively, in the prepared samples. For the BCDs-CTO samples, the optical absorption edge red-shifted to that of CTO, thus evidence that the addition of BCDs widens the light-harvesting capability of the photocatalysts. The enhanced light

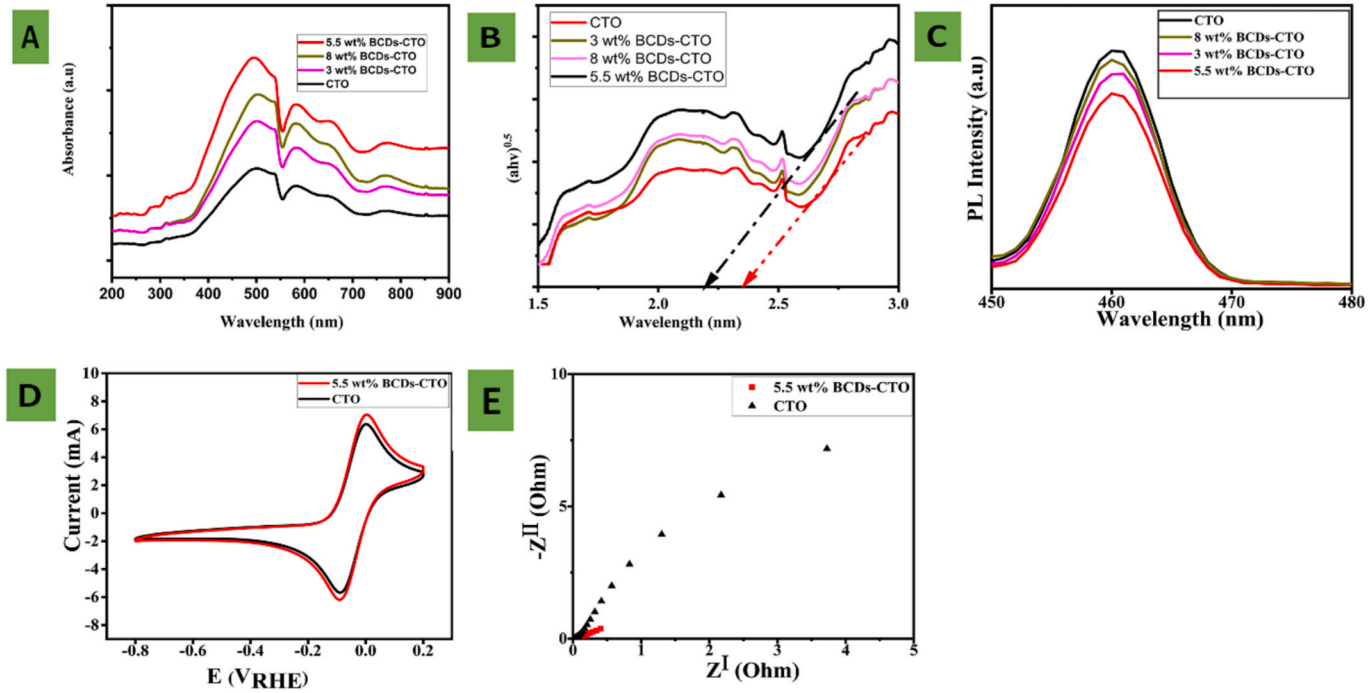

Fig. 5. (A) Absorption spectrum, (B) Tauc's spectra, (C) PL spectra of BCDs-CTO catalysts, and CTO, (D) Cyclic voltammetry, and (E) electrochemical impedance spectra of 5.5 wt% BCDs-CTO, and CTO.

absorption will significantly strengthen the photo generation of charge carriers, and lead to an improved photocatalytic performance (with the 5.5 wt% BCDs-CTO as the most efficient photocatalyst, as evidenced in Section 3.9). The band gap (Eg) of the obtained CTO, and 5.5 wt% BCDs-CTO is approximately 2.33 eV, and 2.20 eV, based on the Tauc plot (Fig. 5**B**). Fig. 5**C** presents the fluorescence spectra of the CTO and BCDs-CTO photocatalysts. The BCDs-CTO photocatalysts have a lower fluorescence intensity (excited at 325 nm) than CTO NM. A lower fluorescence intensity corresponds to high photo-generated charged carrier separation efficiency, so the 5.5 wt% BCDs-9/CTO has the highest separation efficiency. Fig. 5**D and E** shows the CV and EIS of the CTO, and 5.5 wt% BCDs-CTO photocatalysts. The 5.5 wt% BCDs-CTO photocatalyst presented a higher CV curve and smaller EIS radius compared to CTO NM. This indicates higher charge transfer and separation capabilities with the 5.5 wt% BCDs-CTO photocatalyst, thus promoting improved degradation performance. Herein, BCDs inclusion aided an efficient separation of photogenerated charge carriers in the BCDs-CTO photocatalyst, as well as extending their lifecycle.

3.8. Optimization and statistical evaluation on the photocatalytic performance of BCDs-CTO

Three independent variables, catalyst loading (A), pH value (B), and MNZ initial concentration (C), have been used to analyze the degradation factors influence on the removal of MNZ antibiotics, modeled accurately using the central composite design (CCD) through response surface methodology (RSM) is presented in Table 2**.**

As presented in Table S2, optimizing the degradation experimental parameters and MNZ photo-degradation was best achieved through a quadratic model with a lower p-value when compared to other models. The quadratic model equation as suggested by the software with the significant factors, is presented below:

$$\boldsymbol{Degradation of MNZ} = 99.26 - 0.2202A + 0.4338B + 0.2658C + 0.1028AB - 0.9726AC + 0.5370A2 - 1.91C2$$

Fig. 6A–C further presented the validity of the quadratic equation from the CCD-RSM model. The predicted degradation efficiency as a term of actual (MNZ degradation) is illustrated in Fig. 6**A.**, and a high validity of the quadratic model has confirmed strong proximity between variants.

This observation was further confirmed by the normal probability curve versus externally studentized residuals (Fig. 6**B**). The outliers (red threshold) in Fig. 6**C**, evidence no values extend above the model limit expectations, thus highlighting the appropriateness of the regression model. The analysis of variance (ANOVA) in Table 3, presented an F-value of 345.71 and Prob. > F of < 0.0001 justifying the model's significance. The value of Prob. > F less than 0.05 presents the influential model terms, whilst the significance of the parameters for MNZ photo-degradation is A (pH) > B (initial concentration) > C (catalyst loading). This is largely attributed to a higher mean square value. Furthermore, the quadratic model validation from the ANOVA using the (R^2 and adjusted R^2), evidenced good coherence (adjusted $R^2 = 0.9939$, adjusted $R^2 = 0.9857$) [80].

Table 2
Experimental levels for each independent parameter based on RSM design.

Factor	Name	Units	Low Actual	High Actual
A	Catalysts loading	wt %	3	8
B	pH		3	9
C	TC initial Concentration	Mg/L	50	100

The influence of different degradation parameters on the removal of MNZ antibiotics using a 3-dimensional (3D) response surface is presented in Fig. 6D–F. The interaction of pH solution versus the MNZ initial concentration also had a significant influence on the degradation of MNZ antibiotic (*High F value in* Table 3). Increasing the pH solution from 3 to 9 in Fig. 6**F** under optimized conditions at 0.025 g/L photocatalyst dosage, and a degradation time of 60 min, increased the degradation efficiency of MNZ (98.78 % for pH 3 to 99.66 % for pH 9). The initial MNZ concentration's impact on the degradation efficiency is presented in Fig. 6**E and F**. Increasing the MNZ concentration from 50 to 100 mg/L improves the removal efficiency from 96.98 to 97.54 %. Herein, a higher amount of MNZ molecules resulted in more interaction with BCDs-CTO powders, and the formation of active radicals thus yielding higher degradation efficiency [81,82]. With regards to the influence of catalyst loading, as presented in Fig. 6**D and F,** increasing the photocatalyst loading from 3 to 8 wt% resulted in the degradation efficiency reduction from 99.89 to 99.52 %. This is attributed to aggregation on the surface of the CTO, thus shielding the CTO from absorbing the light irradiation, formation of recombination centers for photogenerated charge carriers, and covering the catalytic reactive sites [83].

The final optimization of BCDs-CTO degradation performance on MNZ removal using the desirability function (DF) in this prescribed model is presented in Fig. S3. The predicted outcome (catalyst loading = 5.5, pH = 9, and MNZ = 64.17 mg/L) with degradation efficiency at 99.89 % at 0.765 desirability. This value was utilized for further degradation activities, and the experimental degradation was 99.81 %, and relatively close to the predicted model value of 99.89 %.

3.9. Photocatalytic activities, Scavenging, and recycling

In Fig. 7**A**, the photocatalytic degradation efficiencies of various photocatalysts toward MNZ are depicted. The degradation efficiencies for BCDs, CTO, and 5.5 wt% BCDs-CTO were 51.46 %, 66.56 %, and 99.81 %, after 1 hr irradiation time, respectively. The degradation efficiency of 5.5 wt% BCDs-CTO was higher than that of the CTO, BCDs, and BCDs (5 wt% loading) as a co-catalyst (generation of more electron-hole pairs and reduced electron-hole pair recombination) was responsible for enhancing the performance of CTO in this study. Fig. 7**B** presents the photocatalytic reaction process kinetics, and the pseudo-first-order model [84,85] describes the photocatalytic processes (Eq. (1), with C_0 and C_t are the concentrations of MNZ, respectively, at times t = 0 and t.

$$In\frac{C}{C_O} = -kt \quad (1)$$

Among them, the degradation rate constant of 5.5 wt% BCDs-CTO (0.0786 min^{-1}) surpasses that of CTO (0.0192 min^{-1}) and BCDs (0.0131 min^{-1}) by 4.1 and 6 times, respectively. This signifies an enormous boost in the photocatalytic performance of the heterojunction formed by CTO with BCDs as a co-catalyst. Table S3 depicts the photocatalytic efficiency of BCDs-CTO compared with other photocatalysts in the degradation of MNZ antibiotics in terms of photocatalyst composition, illumination sources, and reaction conditions used [5,86–90]. Herein, the final performance of 5.5 wt% BCDs-CTO is higher than previously reported photocatalysts and thus considered as an efficient photocatalyst for pharmaceutical antibiotics remediation.

The reusability of 5.5 wt% BCDs-CTO nanocomposite was studied for five cycles of MNZ degradation to determine its stability for practical

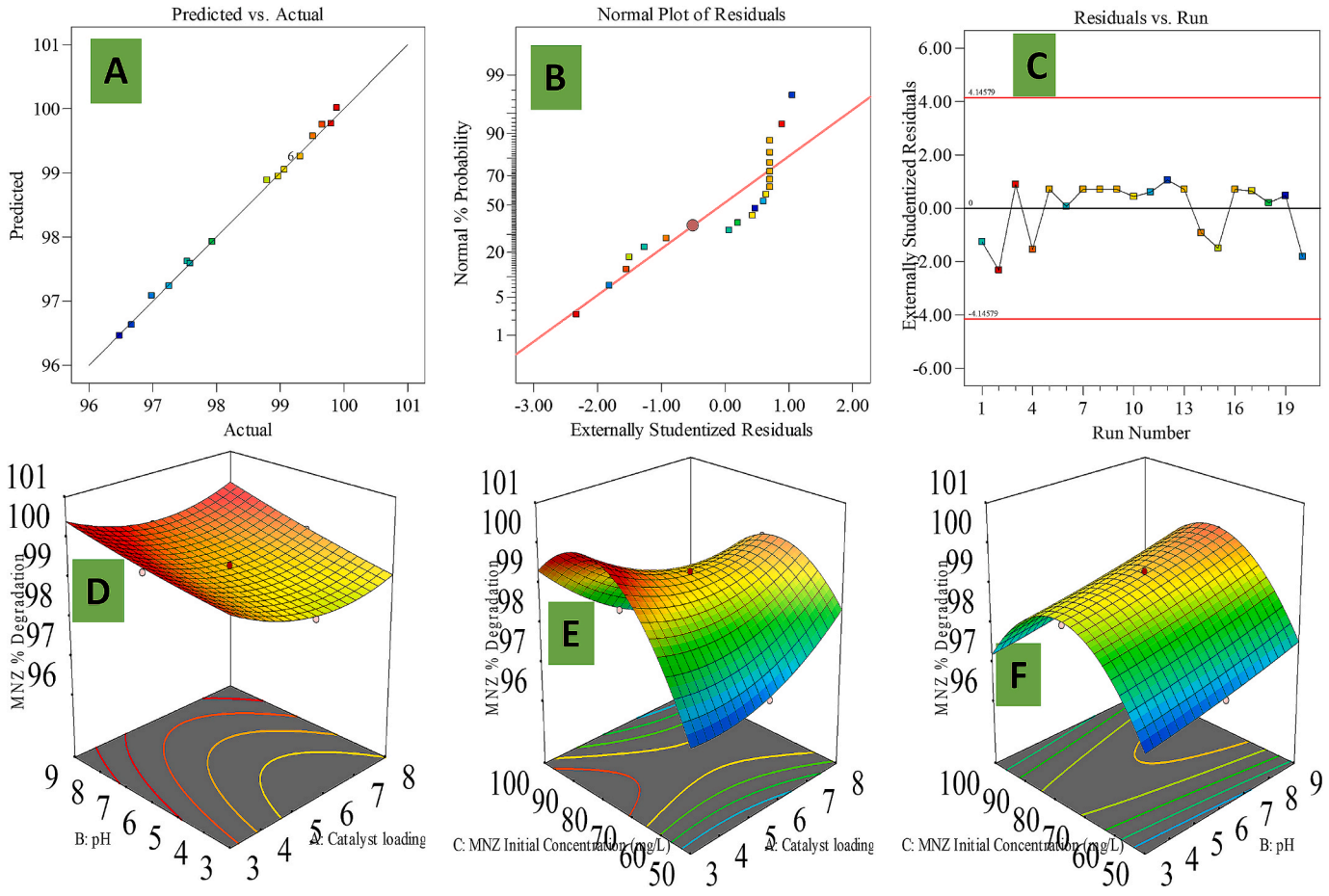

Fig. 6. (A) Predicted vs actual values, (B) Normal probability vs. residuals, and (C) Residual vs. run for BCDs-CTO catalysts on MNZ removal, 3D surface response plots for MNZ photodegradation efficiency on BCDs-CTO catalysts, (D) Effect of pH and catalyst loading, (E) Effect of MNZ concentration and catalyst loading, and (F) Effect of pH and MNZ concentration.

Table 3
Analysis of variance for the degradation of MNZ in the presence of BCDs – CTO nanomaterials.

Source	Sum of Squares	df	Mean Square	F-value	p-value	
Model	23.69	9	2.63	345.71	<0.0001	Significant
A-catalyst loading	0.4848	1	0.4848	63.68	<0.0001	
B-pH	1.88	1	1.88	247.15	<0.0001	
C-concentration	0.7068	1	0.7068	92.83	<0.0001	
AB	0.0846	1	0.0846	11.11	0.0076	
AC	7.57	1	7.57	993.88	<0.0001	
BC	0.0056	1	0.0056	0.7414	0.4094	
A^2	0.7931	1	0.7931	104.17	<0.0001	
B^2	0.0107	1	0.0107	1.41	0.2633	
C^2	9.98	1	9.98	1310.96	<0.0001	
Residual	0.0761	10	0.0076			
Lack of Fit	0.0761	5	0.0152			
Pure Error	0.0000	5	0.0000			
Cor Total	23.76	19				

$R^2 = 0.9939$, R^2 Adjusted $= 0.9857$, R^2 Predicted $= 0.9857$, Adeq Precision $= 57.5855$.

applications. As presented in Fig. 7**C**, the MNZ degradation first run was 99.8 %, while the efficiency for the fifth cycle was 90.86 %. Furthermore, the crystal structure of the fresh, and recycled 5.5 wt% BCDs-CTO sample in Fig. 7**D** demonstrates the stability of the structure, with minimal change after five photocatalytic experiments.

Scavenger quenching experiments were conducted using 5 Mm of benzoquinone (BQ), ethylenediaminetetraacetic Acid Disodium (EDTA-2Na), and isopropanol (IPA) employed to quench superoxide ($O_2^{\bullet-}$), hole (h^+), and hydroxyl (•OH) radical, respectively (Fig. 7**E**). The •OH (76.37 %) exhibited weak inhibition on MNZ degradation (Fig. 7.

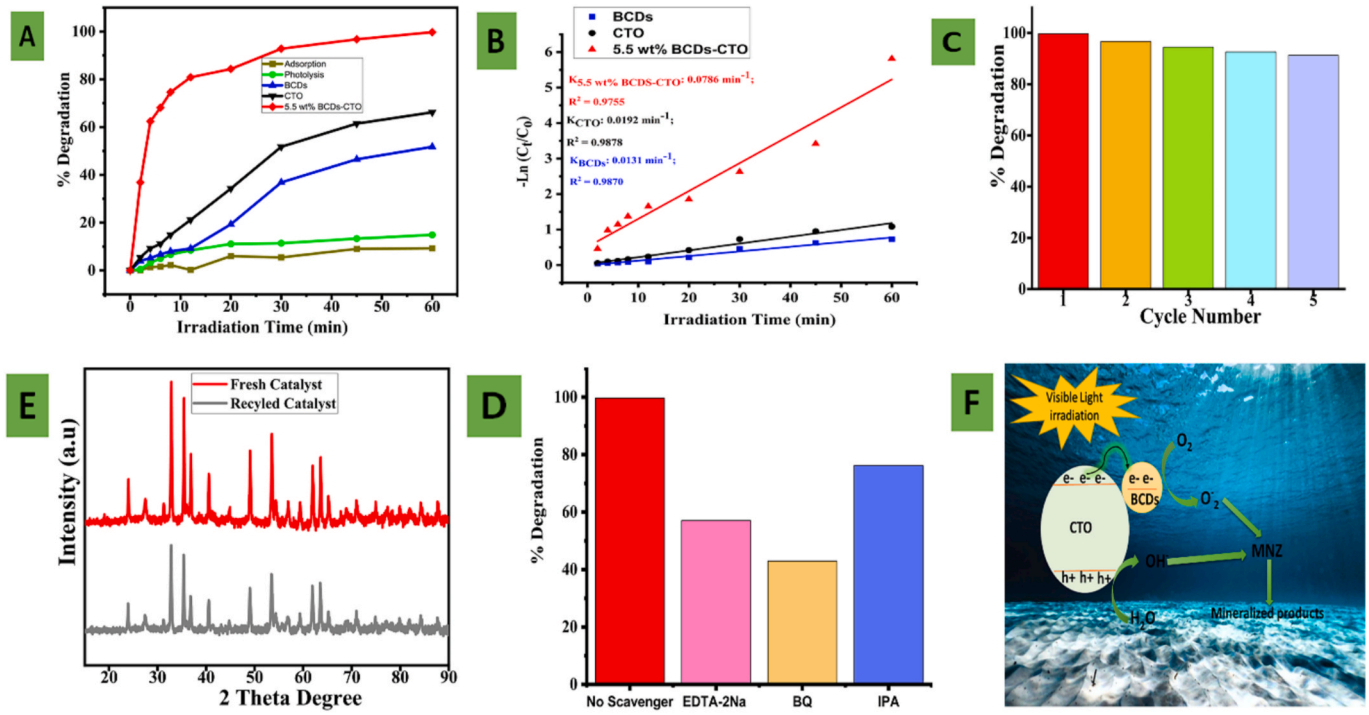

Fig. 7. (A) Photocatalytic performance of 5.5 wt% BCDs-CTO, BCDs, and CTO, (B) Pseudo first-order kinetics, (C) Photocatalyst recycling test, (D) XRD patterns of 5.5 wt% BCDs-CTO, (E) Degradation of MNZ using 5.5 wt% BCDs-CTO in the presence of different scavengers, and (F) Reaction mechanism over BCDs-CTO photo composite in the MNZ degradation.

However, the BQ (43.06 %) addition, as well as EDTA-2Na (57.70 %), significantly inhibited MNZ degradation (Fig. 7C), suggesting that $O_2^{\bullet-}$and h^+ are the primary active species for MNZ degradation with the 5.5 wt% BCDs-CTO photocatalyst.

3.10. Reaction mechanism

The enhanced photodegradation performance of 5.5 wt% BCDs-CTO photocatalyst heterojunction is largely attributed to the incorporation of BCDs into CTO. Hence, the E_{CB} and E_{VB} for the BCDs-CTO photocatalyst were determined with the formulas: $E_{CB} = X - Ee + 0.5Eg$ and $E_{VB} = E_{CB} + Eg$, herein Eg represents the bandgap energy, whilst the electronegativity (X) of pristine CTO (5.76 eV), and Ee symbolized the hydrogen scale-free electron energy (4.5 eV). The E_{VB} and E_{CB} of BCDs-CTO photocatalyst were determined from the above expression to be +2.33 eV and +0.15 eV.

Upon visible light illumination, the CTO catalyst absorbs enough photon energy, thus excites electrons from the VB to CB while leaving h^+ in the VB (Fig. 7**F**). The electrons from the CB of CTO are transferred instantaneously to the BCDs through the BCDs-CTO heterointerface, which then reacts with the surface O_2 to form $O_2^{\bullet-}$, and simultaneously attack the MNZ molecule. Moreover, given the VB of CTO is higher than $OH^-/^{\bullet}OH$ (1.98 ev) the photoinduced h^+ on the VB of CTO could be readily oxidized by the adsorbed H_2O to create •OH, and also attack the pollutant.

4. Conclusions

In summary, the design of water-soluble carbon dots from pine tree bark through microwave pyrolysis for the detection of MNZ was executed in this study. This fabrication method offers several advantages, including simplicity, a greener approach without chemical modification, and utilization of agricultural biomass (crucially adding environmental protection and economic benefits). The prepared BCDs surface functionalities are comprised of diverse functional groups (hydroxy, carboxylic acid, and amino), and possess a strong degree of graphitization. As a result, the BCDs exhibited a favorable quantum yield of 10 %, at an emission of 430 nm under 330 nm excitation. BCDs presented a limit of detection (LOD) of 0.014 μM, via a non-linear detection range spanning from 0 to 25 μM for MNZ. In addition, the application of a BCDs fluorescent probe enabled the measurement of MNZ in authentic water samples, yielding satisfactory results (97–105 %) across all tested samples. In addition, the BCDs modified CTO and utilized as photocatalysts for the degradation of MNZ using the CCD-RSM technique. The BCDs enhanced the visible light absorptivity of BCDs-CTO composites and promoted effective charge carrier transfer. From the ANOVA, it was found that the pH solution has more degree of significance to initial concentration, and catalyst loading in the degradation of MNZ. The maximum degradation activity was obtained about 99.81 % under the specific conditions of pH = 9, MNZ = 64.17 mg/L, and 5.5 wt% catalyst loading during 60-min light irradiation. This significantly improved the photocatalytic performance of the CTO, with an enhanced degradation of the MNZ actualized in this study. Overall, the design of multi-functional nanomaterials achieved sensitive detection and 99.81 % removal of MNZ, thus averting the challenges associated with the usage of mono-functional materials and completely avoiding the hazards of pollutants.

CRediT authorship contribution statement

Saheed O. Sanni: Writing – review & editing, Writing – original draft, Supervision, Methodology, Investigation, Formal analysis, Conceptualization. **Odunayo T. Ore:** Writing – review & editing, Writing – original draft, Visualization, Validation, Resources, Investigation. **Ajibola A. Bayode:** Writing – review & editing, Writing – original draft, Supervision, Software, Investigation, Data curation. **Stephen Sunday Emmanuel:** Writing – review & editing. **Hamza Badamasi:** Writing – review & editing, Writing – original draft, Validation, Investigation.

Funding

There is no funding award to Sanni for this work.

Declaration of competing interest

The authors declare the following financial interests/personal relationships which may be considered as potential competing interests: Saheed O Sanni, Odunayo T. Ore, Ajibola A. Bayode, Stephen Sunday Emmanuel, Hamza Badamasi declare that they have no known competing financial interests or personal relationships that could have appeared to influence the work reported in this paper. If there are other authors, they declare that they have no known competing financial interests or personal relationships that could have appeared to influence the work reported in this paper If there are other authors, they declare that they have no known competing financial interests or personal relationships that could have appeared to influence the work reported in this paper.

Appendix A. Supplementary data

Supplementary data to this article can be found online at https://doi.org/10.1016/j.inoche.2025.114822.

Data availability

Data will be made available on request.

References

[1] B.K. Korah, A.R. Chacko, S. Mathew, B.K. John, T. Abraham, B. Mathew, Biomass-derived carbon dots as a sensitive and selective dual detection platform for fluoroquinolones and tetracyclines, Anal. Bioanal. Chem. 414 (17) (2022) 4935–4951.
[2] C. Han, J. Chen, X. Wu, Y.-W. Huang, Y. Zhao, Detection of metronidazole and ronidazole from environmental samples by surface enhanced Raman spectroscopy, Talanta 128 (2014) 293–298.
[3] X. Wang, T. Lin, W. Wu, H. Wu, D. Yan, Synthesis of N-doped carbon dots for highly selective and sensitive detection of metronidazole in real samples and its cytotoxicity studies, Environ. Technol. 43 (27) (2022) 4213–4226.
[4] G. Ren, X. Hou, Y. Kang, R. Zhang, M. Zhang, W. Liu, L. Li, S. Wei, H. Wang, B. Wang, Efficient preparation of nitrogen-doped fluorescent carbon dots for highly sensitive detection of metronidazole and live cell imaging, Spectrochim. Acta Part A: Mole. Biomolec. Spec. 234 (2020) 118251.
[5] M.L. Tran, C.H. Nguyen, C.-C. Fu, R.-S. Juang, Hybridizing Ag-Doped ZnO nanoparticles with graphite as potential photocatalysts for enhanced removal of metronidazole antibiotic from water, J. Environ. Manage. 252 (2019) 109611.
[6] J. Han, L. Zhang, S. Yang, J. Wang, D. Tan, Detrimental effects of metronidazole on selected innate immunological indicators in common carp (Cyprinus carpio L.), Bull. Environ. Contam. Toxicol. 92 (2014) 196–201.
[7] G. Tiboni, F. Marotta, A. Castigliego, C. Rossi, Impact of estrogen replacement on letrozole-induced embryopathic effects, Human Reprod. 24 (11) (2009) 2688–2692.
[8] D. Chen, J. Deng, J. Liang, J. Xie, C. Hu, K. Huang, A core–shell molecularly imprinted polymer grafted onto a magnetic glassy carbon electrode as a selective sensor for the determination of metronidazole, Sens. Actuat. B: Chem. 183 (2013) 594–600.
[9] K.D. Trivedi, A. Chaudhary, S. Mohan, Devlopment and validation of RP-HPLC method for estimation of metronidazole and norfloxacin in suspension form, Int. J. Adv. Pharm. 2 (2013) 7.
[10] H.M. Maher, R.M. Youssef, R.H. Khalil, S.M. El-Bahr, Simultaneous multiresidue determination of metronidazole and spiramycin in fish muscle using high performance liquid chromatography with UV detection, J. Chrom. B 876 (2) (2008) 175–181.
[11] V.R. Bari, U. Dhorda, M. Sundaresan, Simultaneous estimation of nalidixic acid and metronidazole in dosage forms using packed column supercritical fluid chromatography, Anal. Chimica Acta 376 (2) (1998) 221–225.
[12] M.R. El-Ghobashy, N.F. Abo-Talib, Spectrophotometric methods for the simultaneous determination of binary mixture of metronidazole and diloxanide furoate without prior separation, J. Adv. Res. 1 (4) (2010) 323–329.
[13] U. Gul, S. Kanwal, S. Tabassum, M.A. Gilani, A. Rahim, Microwave-assisted synthesis of carbon dots as reductant and stabilizer for silver nanoparticles with enhanced-peroxidase like activity for colorimetric determination of hydrogen peroxide and glucose, Microchim. Acta 187 (2) (2020) 135.
[14] W. Liu, J. Zhang, C. Li, L. Tang, Z. Zhang, M. Yang, A novel composite film derived from cysteic acid and PDDA-functionalized graphene: enhanced sensing material for electrochemical determination of metronidazole, Talanta 104 (2013) 204–211.
[15] J. Zhao, X. Pan, X. Sun, W. Pan, G. Yu, J. Wang, Detection of metronidazole in honey and metronidazole tablets using carbon dots-based sensor via the inner filter effect, Luminescence 33 (4) (2018) 704–712.
[16] X. Yang, M. Liu, Y. Yin, F. Tang, H. Xu, X. Liao, Green, hydrothermal synthesis of fluorescent carbon nanodots from gardenia, enabling the detection of metronidazole in pharmaceuticals and rabbit plasma, Sensors 18 (4) (2018) 964.
[17] F. Yang, B. Yang, L. He, K. Qi, A. Khataee, Y. Yan, Synthesis of $AgInS_2$ quantum dots for metronidazole detection in eggs using a fluorescence-quenched probe, J. Lumin. 273 (2024) 120673.
[18] W. Wang, S. Li, P. Yin, J. Li, Y. Tang, M. Yang, Response surface methodology optimization for the synthesis of N, S-codoped carbon dots and its application for tetracyclines detection, Chemosphere 303 (2022) 135145.
[19] P. Venugopalan, N. Vidya, Microwave-assisted green synthesis of carbon dots derived from wild lemon (Citrus pennivesiculata) leaves as a fluorescent probe for tetracycline sensing in water, Spectrochim. Acta Part A: Molec. Biomolec. Spectro. 286 (2023) 122024.
[20] P. Yang, Z. Zhu, M. Chen, W. Chen, X. Zhou, Microwave-assisted synthesis of xylan-derived carbon quantum dots for tetracycline sensing, Opt. Mater. 85 (2018) 329–336.
[21] C.R. Thara, B.K. Korah, S. Mathew, B.K. John, B. Mathew, Dual mode detection and sunlight-driven photocatalytic degradation of tetracycline with tailor-made N-doped carbon dots, Environ. Res. 216 (2023) 114450.
[22] A. Mewada, S. Pandey, S. Shinde, N. Mishra, G. Oza, M. Thakur, M. Sharon, M. Sharon, Green synthesis of biocompatible carbon dots using aqueous extract of Trapa bispinosa peel, Mater. Sci. Engineer. C 33 (5) (2013) 2914–2917.
[23] A. Prasannan, T. Imae, One-pot synthesis of fluorescent carbon dots from orange waste peels, Indus. Eng. Chem. Res. 52 (44) (2013) 15673–15678.
[24] P. Singh, S. Kumar, K.S. Kumar, Cl-doped-C-dots and Sg-C3N4 heterojunction for enhanced photocatalytic remediation of dye-polluted wastewater, Biomass Conver. Bioref. (2024) 1–19.
[25] S. Gao, X. Wang, N. Xu, H. Lian, L. Xu, W. Zhang, C. Xu, From coconut petiole residues to fluorescent carbon dots via a green hydrothermal method for Fe3+ detection, Cellulose 28 (3) (2021) 1647–1661.
[26] X. Wang, L. Xu, S. Ge, S.Y. Foong, R.K. Liew, W.W. Fong Chong, M. Verma, M. Naushad, Y.-K. Park, S.S. Lam, Q. Li, R. Huang, Biomass-based carbon quantum dots for polycrystalline silicon solar cells with enhanced photovoltaic performance, Energy 274 (2023) 127354.
[27] T.C. Wareing, P. Gentile, A.N. Phan, Biomass-based carbon dots: current development and future perspectives, ACS Nano 15 (10) (2021) 15471–15501.
[28] L. Yang, L. Zeng, Y. Tao, D. Wang, K. Zhang, M. Tian, Z. Xia, D. Gao, Galli Gigerii Endothelium Corneum derived fluorescent carbon dots and their application as sensing platform for nitroimidazoles and cell imaging, Microchem. J. 174 (2022) 107089.
[29] H. Lv, M. Zhan, G. Li, F. Zhang, Z. Suo, C. Zhou, B. Wan, G. Wang, Y. Liu, Construction of a direct Z-scheme Mn0.5Cd0.5S/CoTiO3 heterojunction with enhanced photocatalytic nitrogen fixation performance, Appl. Surf. Sci. 655 (2024) 159572.
[30] E. Regulska, J. Breczko, A. Basa, Multifunctional NiTiO3-decorated-rGO nanostructure for energy storage, electro- and photocatalytic applications, Diamond Related Mater. 128 (2022) 109310.
[31] Q. Wang, Q. Guo, L. Wang, B. Li, The flux growth of single-crystalline CoTiO3 polyhedral particles and improved visible-light photocatalytic activity of heterostructured CoTiO3/g-C3N4 composites, Dalton Trans. 45 (44) (2016) 17748–17758.
[32] C. Xing, Y. Liu, Y. Zhang, X. Wang, P. Guardia, L. Yao, X. Han, T. Zhang, J. Arbiol, L. Soler, Y. Chen, K. Sivula, N. Guijarro, A. Cabot, J. Llorca, A direct Z-scheme for the photocatalytic hydrogen production from a water ethanol mixture on CoTiO3/TiO2 heterostructures, ACS Appl. Mater. Interf. 13 (1) (2021) 449–457.
[33] G. Dong, K. Lang, Y. Gao, W. Zhang, D. Guo, J. Li, D.-F. Chai, L. Jing, Z. Zhang, Y. Wang, A novel composite anode via immobilizing of Ce-doped PbO2 on CoTiO3 for efficiently electrocatalytic degradation of dye, J. Colloid Interf. Sci. 608 (2022) 2921–2931.
[34] M.R. Pallavolu, N. Gaddam, A.N. Banerjee, R.R. Nallapureddy, Y.A. Kumar, S. W. Joo, Facile construction and controllable design of CoTiO3@Co3O4/NCNO hybrid heterojunction nanocomposite electrode for high-performance supercapacitors, Electrochim. Acta 407 (2022) 139868.
[35] C.A. Ha, D.T. Nguyen, T. Nguyen, Green fabrication of heterostructured CoTiO3/TiO2 nanocatalysts for efficient photocatalytic degradation of cinnamic acid, ACS Omega 7 (44) (2022) 40163–40175.

[36] J. Wei, J. Bi, L. Zhang, D. Han, J. Gong, Gravity-driven Fe-doped CoTiO3/SiO2 fiber membrane with open catalytic network: activation of peroxymonosulfate and efficient pollutants removal, Sep. Purif. Technol. 280 (2022) 119975.
[37] L. Wang, P. Cai, Z. Liu, Z. Xie, Y. Fang, Role of carbon quantum dots on Nickel titanate to promote water oxidation reaction under visible light illumination, J. Coll. Interf. Sci. 607 (2022) 203–209.
[38] H. Kooshki, A. Sobhani-Nasab, M. Eghbali-Arani, F. Ahmadi, V. Ameri, M. Rahimi-Nasrabadi, Eco-friendly synthesis of PbTiO3 nanoparticles and PbTiO3/carbon quantum dots binary nano-hybrids for enhanced photocatalytic performance under visible light, Sep. Purif. Technol. 211 (2019) 873–881.
[39] R. Xie, Y. Song, F. Wang, J. Li, X. Zhang, H. Zou, Detection and elimination of tetracycline: Constructing multi-mode carbon dots for ultra-sensitive visual assay and CDs/TiO_2 for photocatalytic degradation, Appl. Surf. Sci. 648 (2024) 158990.
[40] K. Qi, C. Imparato, O. Almjasheva, A. Khataee, W. Zheng, TiO_2-based photocatalysts from type-II to S-scheme heterojunction and their applications, J. Coll. Interf. Sci. 675 (2024) 150–191.
[41] J. Zhang, Y. Zhao, K. Qi, S.-Y. Liu, CuInS2 quantum-dot-modified g-C3N4 S-scheme heterojunction photocatalyst for hydrogen production and tetracycline degradation, J. Mater. Sci. Technol. 172 (2024) 145–155.
[42] E.O. Oseghe, T.A. Msagati, B.B. Mamba, A.E. Ofomaja, An efficient and stable narrow bandgap carbon dot-brookite composite over other CD-TiO2 polymorphs in rhodamine B degradation under LED light, Ceram. Inter. 45 (11) (2019) 14173–14181.
[43] V. Dhyani, T. Bhaskar, A comprehensive review on the pyrolysis of lignocellulosic biomass, Renew. Energy 129 (2018) 695–716.
[44] J. Tang, Y. Zhang, Y. Liu, D. Liu, H. Qin, N. Lian, Carbon quantum dots as a fluorophore for "inner filter effect" detection of metronidazole in pharmaceutical preparations, RSC Adv. 9 (65) (2019) 38174–38182.
[45] J.-H. Zhang, A. Niu, J. Li, J.-W. Fu, Q. Xu, D.-S. Pei, In vivo characterization of hair and skin derived carbon quantum dots with high quantum yield as long-term bioprobes in zebrafish, Sci. Rep. 6 (1) (2016) 37860.
[46] S. Mathew, C.R. Thara, N. John, B. Mathew, Carbon dots from green sources as efficient sensor and as anticancer agent, J. Photochem. Photobiol. A: Chem.4 434 (2023) 114237.
[47] H. Wu, L.-F. Pang, M.-J. Fu, X.-F. Guo, H. Wang, Boron and nitrogen codoped carbon dots as fluorescence sensor for Fe3+ with improved selectivity, J. Pharmac. Biomed. Anal. 180 (2020) 113052.
[48] F. Nemati, M. Hosseini, R. Zare-Dorabei, F. Salehnia, M.R. Ganjali, Fluorescent turn on sensing of Caffeine in food sample based on sulfur-doped carbon quantum dots and optimization of process parameters through response surface methodology, Sens. Actuat. B: Chem. 273 (2018) 25–34.
[49] H. Ma, L. Guan, M. Chen, Y. Zhang, Y. Wu, Z. Liu, D. Wang, F. Wang, X. Li, Synthesis and enhancement of carbon quantum dots from Mopan persimmons for Fe3+ sensing and anti-counterfeiting applications, Chem. Engineer. J. 453 (2023) 139906.
[50] A. Muthurasu, V. Ganesh, Tuning optical properties of nitrogen-doped carbon dots through fluorescence resonance energy transfer using Rhodamine B for the ratiometric sensing of mercury ions, Anal. Methods 13 (15) (2021) 1857–1865.
[51] P. Sun, W. Song, Y. Zou, M. Tian, F. Zhang, F. Chai, The fabrication of N-doped carbon dots by methionine and their utility in sensing Cu 2+ in real water, Anal. Methods 15 (13) (2023) 1631–1638.
[52] S. Mondal, C. Vinod, U.K. Gautam, 'Autophagy'and unique aerial oxygen harvesting properties exhibited by highly photocatalytic carbon quantum dots, Carbon 181 (2021) 16–27.
[53] R. Atchudan, T.N.J.I. Edison, S. Perumal, N. Muthuchamy, Y.R. Lee, Hydrophilic nitrogen-doped carbon dots from biowaste using dwarf banana peel for environmental and biological applications, Fuel 275 (2020) 117821.
[54] R. Gao, Z. Wu, L. Wang, J. Liu, Y. Deng, Z. Xiao, J. Fang, Y. Liang, Green preparation of fluorescent nitrogen-doped carbon quantum dots for sensitive detection of oxytetracycline in environmental samples, Nanomaterials 10 (8) (2020) 1561.
[55] S.O. Sanni, T.H. Moundzounga, E.O. Oseghe, N.H. Haneklaus, E.L. Viljoen, H. G. Brink, One-step green synthesis of water-soluble fluorescent carbon dots and its application in the detection of Cu^{2+}, Nanomaterials 12 (6) (2022) 958.
[56] S. Zhao, X. Song, X. Chai, P. Zhao, H. He, Z. Liu, Green production of fluorescent carbon quantum dots based on pine wood and its application in the detection of Fe3+, J. Cleaner Produc. 263 (2020) 121561.
[57] A.C.C. Pena, L.M. Raymundo, L.F. Trierweiler, M. Gutterres, Green carbon dots synthesized from Chlorella Sorokiniana microalgae biochar for chrome detection, J. Indus. Engineer. Chem. 117 (2023) 130–139.
[58] D. Zhang, F. Zhang, S. Wang, S. Hu, Y. Liao, F. Wang, H. Liu, Red-to-blue colorimetric probe based on biomass carbon dots for smartphone-integrated optosensing of Cu(II) and L-cysteine, Spectrochim, Acta Part A: Molec. Biomolec. Spectro. 290 (2023) 122285.
[59] A. Inayat, K. Albalawi, A.-U. Rehman, A.Y. Adnan, E.A.M. Saad, M.A. Saleh, A. A. Alamri, A. El-Zahhar, S.M.A. Haider, Tunable synthesis of carbon quantum dots from the biomass of spent tea leaves as supercapacitor electrode, Mater. Today Commun. 34 (2023) 105479.
[60] Z. Li, Y. Cao, T. Feng, T. Wei, C. Xue, Z. Li, J. Xu, Nitrogen-doped carbon dots/Fe 3 +-based fluorescent probe for the "off–on" sensing of As (v) in seafood, Anal. Methods 15 (15) (2023) 1923–1931.
[61] S. Wang, H. Zhao, J. Yang, Y. Dong, S. Guo, Q. Cheng, Y. Li, S. Liu, Preparation of multicolor biomass carbon dots based on solvent control and their application in Cr (VI) detection and advanced anti-counterfeiting, ACS Omega 8 (7) (2023) 6550–6558.
[62] P. Zhu, K. Tan, Q. Chen, J. Xiong, L. Gao, Origins of efficient multiemission luminescence in carbon dots, Chem. Mater.3 31 (13) (2019) 4732–4742.
[63] Q. Zhang, R. Wang, B. Feng, X. Zhong, K. Ostrikov, Photoluminescence mechanism of carbon dots: triggering high-color-purity red fluorescence emission through edge amino protonation, Nature Commun. 12 (1) (2021) 6856.
[64] H. Ren, Y. Yuan, A. Labidi, Q. Dong, K. Zhang, E. Lichtfouse, A.A. Allam, J. S. Ajarem, C. Wang, Green process of biomass waste derived fluorescent carbon quantum dots for biological imaging in vitro and in vivo, Chinese Chem. Lett. 34 (6) (2023) 107998.
[65] W. Wang, C. Damm, J. Walter, T.J. Nacken, W. Peukert, Photobleaching and stabilization of carbon nanodots produced by solvothermal synthesis, Phys. Chem. Chem. Phys. 18 (1) (2016) 466–475.
[66] I.H.T. Guideline, Validation of Analytical Procedures: Text and Methodology Q2 (R1) 1(20) (2005) 05.
[67] Y. Mu, Q. Zhuang, S. Huang, M. Hu, Y. Wang, Y. Ni, Adenine-stabilized carbon dots for highly sensitive and selective sensing of copper (II) ions and cell imaging, Spectrochim, Acta Part A: Molec. Biomolec. Spectro. 239 (2020) 118531.
[68] S. Bhatt, M. Bhatt, A. Kumar, G. Vyas, T. Gajaria, P. Paul, Green route for synthesis of multifunctional fluorescent carbon dots from Tulsi leaves and its application as Cr(VI) sensors, bio-imaging and patterning agents, Coll. Surfaces B: Biointerf. 167 (2018) 126–133.
[69] S. Yang, L. Wang, L. Zuo, C. Zhao, H. Li, L. Ding, Non-conjugated polymer carbon dots for fluorometric determination of metronidazole, Microchim. Acta 186 (9) (2019) 652.
[70] G. Ren, X. Hou, Y. Kang, R. Zhang, M. Zhang, W. Liu, L. Li, S. Wei, H. Wang, B. Wang, H. Diao, Efficient preparation of nitrogen-doped fluorescent carbon dots for highly sensitive detection of metronidazole and live cell imaging, Spectrochim, Acta Part A: Molec. Biomolec. Spectro. 234 (2020) 118251.
[71] N. Yalikun, X. Mamat, Y. Li, X. Hu, P. Wang, G. Hu, N, S, P-triple doped porous carbon as an improved electrochemical sensor for metronidazole determination, J. Electrochem. Soc. 166 (13) (2019) B1131.
[72] H. Qi, L. Qiu, X. Zhang, T. Yi, J. Jing, R. Sami, S.F. Alanazi, Z. Alqahtani, M. D. Aljabri, M.M. Rahman, Novel N-doped carbon dots derived from citric acid and urea: fluorescent sensing for determination of metronidazole and cytotoxicity studies, RSC Adv. 13 (4) (2023) 2663–2671.
[73] M. Saranya Devi, T. Daniel Thangadurai, D. Nataraj, K. Naveen Kumar, Bismuth-doped carbon quantum dots as an effective fluorescent probe for metronidazole detection through inner filter effect, cytotoxicity studies, and bioimaging in Zebrafish, J. Photochem. Photobiol. A Chem. 450 (2024) 115429.
[74] P.C. Hernández-Del Castillo, G. Robledo-Trujillo, V. Rodríguez-González, Development of a visible-light-active-NiTiO3 coating for the efficient removal of the persistent herbicide 2,6-dichlorobenzamide (BAM) from drinking water, Chemosphere 339 (2023) 139628.
[75] B. Ohtani, Titania Photocatalysis beyond Recombination: a critical Review, Catalysts (2013) 942–953.
[76] R. Dadigala, R. Bandi, M. Alle, B.R. Gangapuram, V. Guttena, J.-C. Kim, In-situ fabrication of novel flower like MoS2/CoTiO3 nanorod heterostructures for the recyclable degradation of ciprofloxacin and bisphenol a under sunlight, Chemosphere 281 (2021) 130822.
[77] Y. Liu, J. Wu, X. Li, J. Chen, Y. Li, X. Luo, T. Xie, Q. Qiu, T. Liang, Highly efficient CoTiO3/MOF-derived In2S3 photo-electrocatalysts: Degradation kinetics, pathways, and mechanism, J. Alloys Comp. 975 (2024) 172921.
[78] R. Ye, H. Fang, Y.-Z. Zheng, N. Li, Y. Wang, X. Tao, Fabrication of CoTiO3/g-C3N4 Hybrid Photocatalysts with Enhanced H2 Evolution: Z-Scheme Photocatalytic Mechanism Insight, ACS Appl. Mater. Interf.8 8 (22) (2016) 13879–13889.
[79] L. Gou, W.-Q. Wang, E.-Z. Liu, L. Xu, R. He, Y. Yang, Fabrication of MOF-derived CoTiO3/g-C3N4 S-scheme heterojunction for photocatalyst wastewater treatment, J. Alloys Comp. 918 (2022) 165698.
[80] M. Sohrabian, V. Mahdikhah, E. Alimohammadi, S. Sheibani, Improved photocatalytic performance of SrTiO3 through a Z-scheme polymeric-perovskite heterojunction with g-C3N4 and plasmonic resonance of Ag mediator, Appl. Surf. Sci. 618 (2023) 156682.
[81] W. Dong, G. Chen, X. Hu, X. Zhang, W. Shi, Z. Fu, Molybdenum disulfides nanoflowers anchoring iron-based metal organic framework: a synergetic catalyst with superior peroxidase-mimicking activity for biosensing, Sens. Actuat. B: Chem. 305 (2020) 127530.
[82] M. Ebadi, M. Asri, F. Beshkar, Novel Mo/Bi2MoO6/Bi3ClO4 heterojunction photocatalyst for ultra-deep desulfurization of thiophene under simulated sunlight irradiation, Adv. Powder Technol. 32 (7) (2021) 2160–2170.
[83] H. Ren, F. Qi, A. Labidi, J. Zhao, H. Wang, Y. Xin, J. Luo, C. Wang, Chemically bonded carbon quantum dots/Bi2WO6 S-scheme heterojunction for boosted photocatalytic antibiotic degradation: Interfacial engineering and mechanism insight, Appl. Catal. B: Environ. 330 (2023) 122587.
[84] O.K. Mmelesi, S. Ammar-Merah, T.T.I. Nkambule, B. Nkosi, X. Liu, K.K. Kefeni, A. T. Kuvarega, The photodegradation of naproxen in an aqueous solution employing a cobalt ferrite-carbon quantum dots (CF/N-CQDs) nanocomposite, synthesized via microwave approach, J. Water Proc. Eng. 59 (2024) 104968.
[85] D.E. Moshoeu, S.O. Sanni, E.O. Oseghe, T.A. Msagati, B.B. Mamba, A.E. Ofomaja, Morphological influence of TiO2 nanostructures on charge transfer and tetracycline degradation under LED light, Chem. Select 5 (3) (2020) 1037–1040.
[86] E. Asgari, A. Esrafili, A.J. Jafari, R.R. Kalantary, H. Nourmoradi, M. Farzadkia, The comparison of ZnO/polyaniline nanocomposite under UV and visible radiations for decomposition of metronidazole: Degradation rate, mechanism and mineralization, Proc. Safety Environ. Protec. 128 (2019) 65–76.

[87] F. Heidarinejad, H. Kamani, A. Khtibi, Magnetic Fe-doped TiO2@Fe3O4 for metronidazole degradation in aqueous solutions: Characteristics and efficacy assessment, Heliyon 9 (11) (2023) e21414.
[88] F. Ghribi, M. Sehailia, L. Aoudjit, F. Touahra, D. Zioui, A. Boumechhour, D. Halliche, K. Bachari, Z. Benmaamar, Solar-light promoted photodegradation of metronidazole over ZnO-ZnAl2O4 heterojunction derived from 2D-layered double hydroxide structure, J. Photochem. Photobiol. A Chem. 397 (2020) 112510.
[89] E. Asgari, A. Esrafili, A.J. Jafari, R.R. Kalantary, M. Farzadkia, Synthesis of TiO2/polyaniline photocatalytic nanocomposite and its effects on degradation of metronidazole in aqueous solutions under UV and visible light radiation, Desalin. Water Treat. 161 (2019) 228–242.
[90] H. Cai, D. Zhang, X. Ma, Z. Ma, A novel ZnO/biochar composite catalysts for visible light degradation of metronidazole, Sep. Purif. Technol. 288 (2022) 120633.

Dr Saheed Sanni is an excellent researcher in the field of photocatalysis, materials engineering, adsorption and detection studies. Over the past seven years, his work has significantly contributed to advancing sustainable technologies, circular economy solutions, and nanomaterial applications, bridging academic innovation with real-world impact. For the past five years, Dr. Saheed Sanni has been a Principal Investigator of the National Research Foundation of South Africa (Project Nos. 99330 and 111330) as well as the University of Sasol Collaborative Program. He has also received a research grant from Sichuan University of Science and Technology (24007). His research results have been published in academic platforms such as Science Direct (Journal of Molecular Liquids, and Process Safety and Environmental Protection), Springer (Adsorption, Catalysis Letters), and RSC Advances. Dr. Sani presented his research results in the form of oral and poster presentations at the International Conference on Environmental Catalysis in Tianjin, China, in 2018, and the Nano Today Conference in Hawaii, USA, in 2017.